THE JOURNAL OF PHYSICAL CHEMISTRY A
A JOURNAL OF THE AMERICAN CHEMICAL SOCIETY

pubs.acs.org/JPCA

Article

Anisotropic Interlayer Force Field for Group-VI Transition Metal Dichalcogenides

Published as part of The Journal of Physical Chemistry A virtual special issue "Gustavo Scuseria Festschrift".

Wenwu Jiang,[¶] Reut Sofer,[¶] Xiang Gao,[¶] Alexandre Tkatchenko, Leeor Kronik, Wengen Ouyang,* Michael Urbakh,* and Oded Hod

Cite This: *J. Phys. Chem. A* 2023, 127, 9820−9830

Read Online

ACCESS | Metrics & More | Article Recommendations | Supporting Information

ABSTRACT: An anisotropic interlayer force field that describes the interlayer interactions in homogeneous and heterogeneous interfaces of group-VI transition metal dichalcogenides (MX_2, where M = Mo, W, and X = S, Se) is presented. The force field is benchmarked against density functional theory calculations for bilayer systems within the Heyd−Scuseria−Ernzerhof hybrid density functional approximation, augmented by a nonlocal many-body dispersion treatment of long-range correlation. The parametrization yields good agreement with the reference calculations of binding energy curves and sliding potential energy surfaces. It is found to be transferable to transition metal dichalcogenide (TMD) junctions outside of the training set that contain the same atom types. Calculated bulk moduli agree with most previous dispersion-corrected density functional theory predictions, which underestimate the available experimental values. Calculated phonon spectra of the various junctions under consideration demonstrate the importance of appropriately treating the anisotropic nature of the layered interfaces. Considering our previous parametrization for MoS_2, the anisotropic interlayer potential enables accurate and efficient large-scale simulations of the dynamical, tribological, and thermal transport properties of a large set of homogeneous and heterogeneous TMD interfaces.

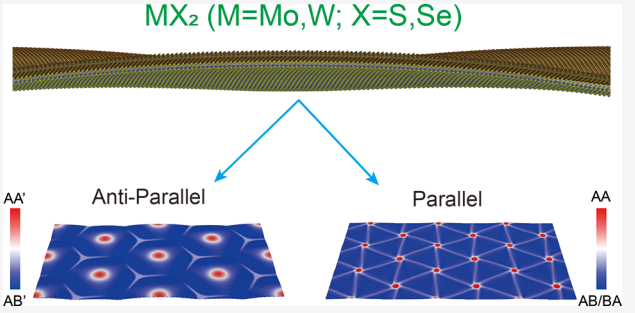

1. INTRODUCTION

Motivated by the fascinating physical properties of graphene, the study of alternative semiconducting two-dimensional (2D) layered materials, in particular the vast family of transition metal dichalcogenides (TMDs), has seen tremendous growth in the past decade.[1] TMDs are characterized by the general chemical formula MX_2, where M is a transition metal atom (e.g., Mo or W), and X is a chalcogen atom (e.g., S, Se, or Te). The formation of moiré superlattices at heterogeneous or misaligned homogeneous TMD interfaces leads to many unique electrical,[2−6] optical,[7−9] thermal,[10−14] and tribological[15−19] properties. Notably, the most interesting physics arises at interfaces characterized by a small lattice mismatch, which is either intrinsic to the contacting materials or enforced via interfacial misalignment. This, in turn, results in relatively large moiré supercell dimensions, which are difficult to model through first-principles calculations. A viable alternative is the use of classical interlayer force fields, which, in the case of 2D materials, have to include a dedicated term that accounts for the anisotropic nature of the layered construct, characterized by a covalent intralayer network and weaker dispersive interlayer interactions. When appropriately parametrized against state-of-the-art density functional theory (DFT) reference data sets, such force fields, known as interlayer potentials (ILPs), provide a desirable balance between accuracy and computational efficiency.[20−28]

Various density functional approximations that address dispersion interactions have been successfully used for generating reference data against which ILPs have been parametrized for a variety of layered material contacts.[20−28] These include the nonlocal (NL) vdW-DF-C09,[29] as well as DFT+D,[30,31] Tkatchenko−Scheffler (TS),[32] many-body dispersion (MBD),[33,34] and MBD-NL[35] dispersion-augmented functionals. The obtained ILPs have proven to provide good agreement with structural,[36−39] mechanical,[27,40−42] tribological,[25,43−51] and thermal transport[27,52−54] experimental observations of layered contacts, and have demonstrated predictive power, that has led to novel experimental findings.[43,44,55] Notably, the previous Kolmogorov−Crespi

Received: July 6, 2023
Revised: September 21, 2023
Published: November 8, 2023

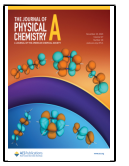

https://doi.org/10.1021/acs.jpca.3c04540
J. Phys. Chem. A 2023, 127, 9820−9830

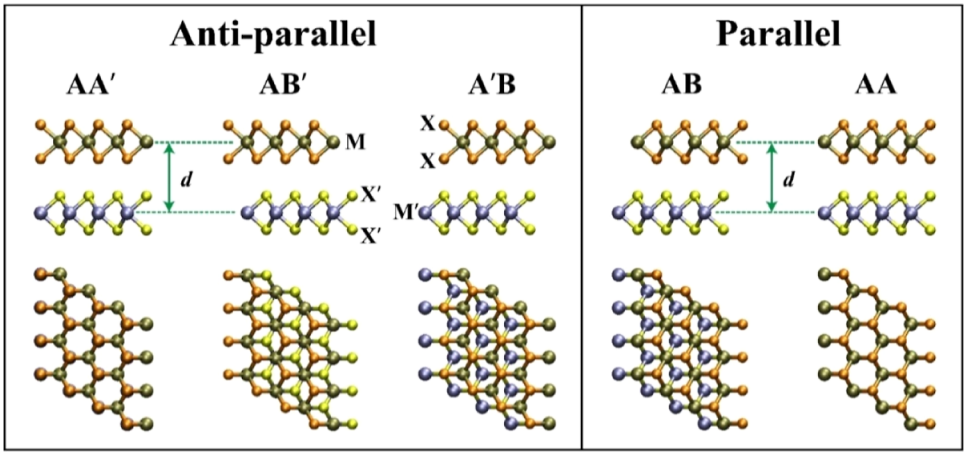

Figure 1. Schematic of the high symmetry stacking modes of bilayer TMD homo- and heterojunctions $(MX_2)/(M'X_2')$ considered for BE curve calculations. For clarity of presentation, atoms residing in different layers are shown in different colors.

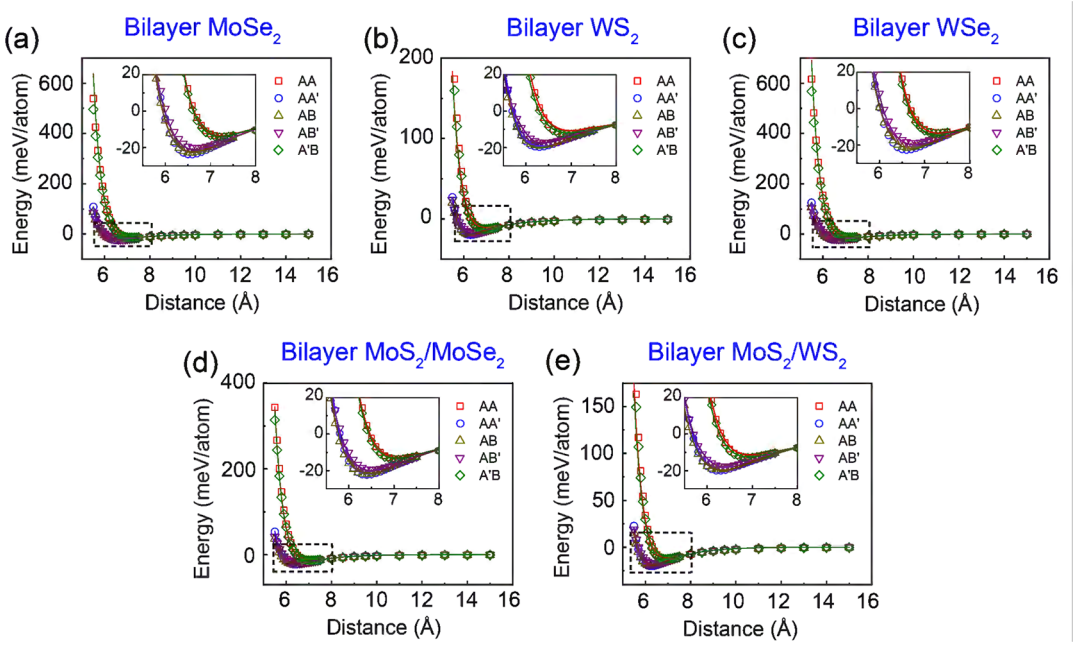

Figure 2. BE curves for three homojunction bilayers: (a) $MoSe_2$, (b) WS_2, and (c) WSe_2, and two heterojunction bilayers: (d) $MoS_2/MoSe_2$, and (e) MoS_2/WS_2, calculated at the HSE + MBD-NL level of DFT (open symbols), along with the corresponding ILP fits (solid lines). Three stacking modes of the antiparallel configuration (AA′—blue circles, AB′—purple inverted triangles, and A′B—green diamonds) and two stacking modes of the parallel configuration (AB—tan triangles, and AA—red squares) are considered (see Figure 1). The parameters presented in Table S1 in Supporting Information Section 3 are used to perform the ILP calculations. The reported energies are measured relative to the values of the two monolayers and are normalized by the total number of atoms in the unit cell (6 atoms). The insets provide a zoomed-in view of the equilibrium interlayer distance region, marked by dashed black rectangles.

type anisotropic potentials have been parametrized for TMD interfaces against DFT reference data at the level of the local density approximation (LDA) augmented by the nonlocal vdW-DF-C09 density functional.[26] While the developed force-field provided a satisfactory description of moiré superlattice structural transformations in twisted bilayer MoS_2,[26] this approach is known to overestimate the binding energy (BE) of MoS_2, graphite, and *h*-BN by ∼40%.[28,56]

Here, we extend our anisotropic ILP parametrization to TMD interfaces consisting of tungsten (W) and selenide (Se) using MBD-NL DFT reference data that were shown to account well for long-range dispersion interactions in polarizable interfaces.[35] Taken together with our previous parametrization for MoS_2 stacks,[28] the new ILP capabilities now allow for a description of interlayer interactions in any homogeneous or heterogeneous MX_2 type junctions, where M = Mo and W and X = S and Se.

2. METHODOLOGY

2.1. DFT Calculations. The reference data set includes a series of BE curves and sliding potential energy surfaces (PESs), calculated for homogeneous and heterogeneous TMD bilayers. The bilayer configurations, have been constructed by rigidly stacking and shifting two preoptimized monolayers. BE curves for each bilayer junction have been calculated at five high-symmetry stacking modes, two parallel (P) modes (AB and AA), and three antiparallel (AP) modes (AA′, AB′, and A′B), as shown in Figure 1. The interlayer distance has been

https://doi.org/10.1021/acs.jpca.3c04540
J. Phys. Chem. A 2023, 127, 9820−9830

Table 1. Equilibrium Interlayer Distances, d_{eq} (Å) and Binding Energies, E_b (meV/atom), for $MoSe_2$, WS_2, and WSe_2 Bilayers, Calculated at Several Stacking Modes Using Various DFT Methods and the ILPs Constructed in This Work[a]

methods			RPA[61]		PBE + D2[61]		HSE06 + MBD-NL (this work)		ILP-MBD-NL (this work)	
stacking modes (bilayer)			d_{eq}	E_b	d_{eq}	E_b	d_{eq}	E_b	d_{eq}	E_b
$MoSe_2$	anti-parallel configurations	AA′	6.48	29.5	6.53	35.6	6.6	23.7	6.6	22.7
		AB′	6.53	25.4	6.63	31.9	6.7	20.2	6.7	21.2
		A′B	7.12	16.7	7.10	22.2	7.2	14.2	7.2	13.8
	parallel configurations	AB	6.47	28.4	6.53	35.1	6.6	22.9	6.6	22.5
		AA	7.18	17.2	7.13	14.4	7.3	13.8	7.2	13.4
WS_2	anti-parallel configurations	AA′	6.24	27.6	6.24	30.2	6.3	19.7	6.4	19.2
		AB′	6.27	22.3	6.24	27.0	6.4	17.2	6.4	17.4
		A′B	6.78	14.8	6.80	19.3	6.9	12.7	6.9	11.8
	parallel configurations	AB	6.24	24.8	6.24	29.6	6.3	19.1	6.3	19.8
		AA	6.84	14.6	6.84	18.9	6.9	12.4	7.0	10.6
WSe_2	anti-parallel configurations	AA′	6.50	30.3	6.54	42.0	6.6	22.6	6.7	21.8
		AB′	6.62	24.5	6.59	37.3	6.8	18.8	6.8	19.8
		A′B	7.24	16.1	7.08	26.3	7.3	13.6	7.3	14.4
	parallel configurations	AB	6.54	28.1	6.54	40.9	6.6	21.5	6.7	21.8
		AA	7.24	16.2	7.09	25.5	7.3	13.2	7.3	13.5

[a]Intralayer hexagonal lattice constants of 3.26, 3.16, and 3.27 Å are used for $MoSe_2$, WS_2, and WSe_2, respectively.

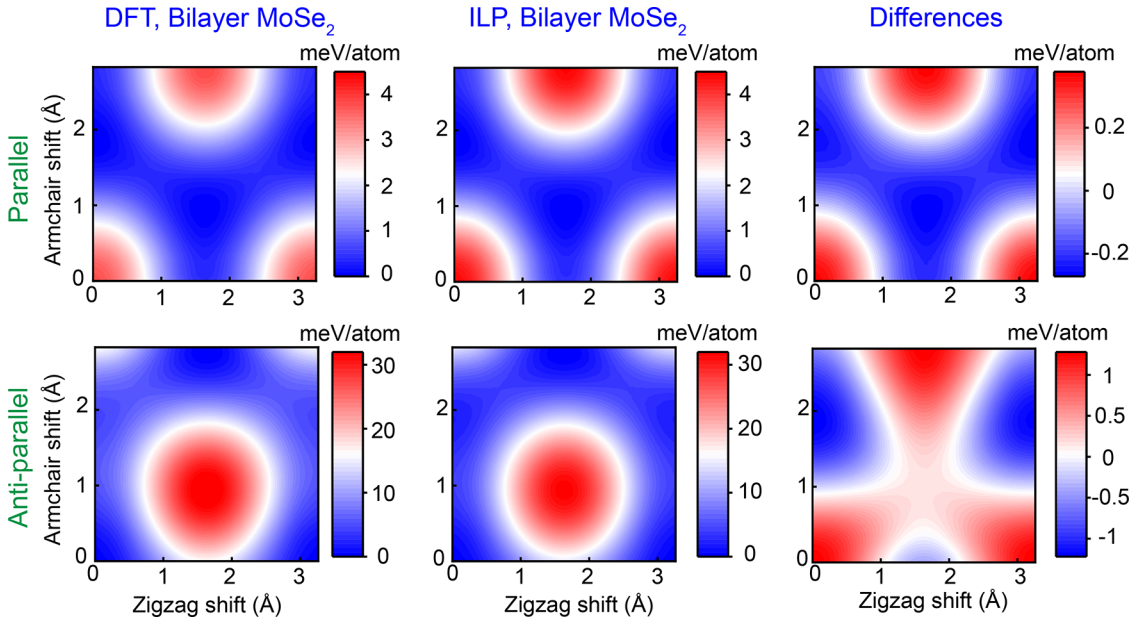

Figure 3. Sliding energy surfaces of bilayer $MoSe_2$, calculated at interlayer distances of 7.2 Å for the parallel (top panels) and 6.5 Å for the antiparallel (bottom panels) configurations. The left and middle columns present DFT (HSE + MBD-NL) and ILP PESs, respectively, and the right column presents their difference maps. The parameters presented in Table S1 in Supporting Information Section 3 are used for the ILP calculations. The reported energies are normalized by the total number of atoms in the unit cell (6 atoms) and measured relative to the values obtained at the AB and AA′ stacking modes for the parallel and antiparallel configurations, respectively.

varied in the range of 5.5−15 Å, including the sub-equilibrium regime, which is important for the investigation of tribological properties. Each BE curve and sliding PES contains 31 and 132 data points, respectively. We note that the reference DFT data set excludes twisted interfaces that are characterized by large supercells, the PES calculation of which requires substantial computational efforts. Such interfaces, however, exhibit potential energy barriers that are 2 orders of magnitude smaller than those obtained for 2*H*-stacked MoS_2 bilayers[57] and are of the order of the expected accuracy of our DFT calculations. Therefore, their inclusion in the training data set does not have a significant impact on the ILP parametrization. This assertion is further justified in Section 4.4 below, where the developed ILP is shown to nicely reproduce the reconstructed structure of twisted suspended MoS_2 bilayers.

All calculations were performed using the FHI-AIMS code.[58] The HSE functional,[59] augmented by the MBD-NL dispersion correction,[35] has been used with the tier-2 basis-set[60] and tight convergence settings with all grid divisions and a denser outer grid. The atomic zeroth-order regular approximation was employed to describe relativistic effects in the vicinity of the nucleus.[58] A *k*-point grid of 19 × 19 × 1 was used, with a vacuum size of 100 Å to prevent spurious interactions with neighboring image cells. Convergence tests of the calculation parameters are provided in Section 1 of the Supporting Information. We note that the bilayer reference data are

https://doi.org/10.1021/acs.jpca.3c04540
J. Phys. Chem. A 2023, 127, 9820−9830

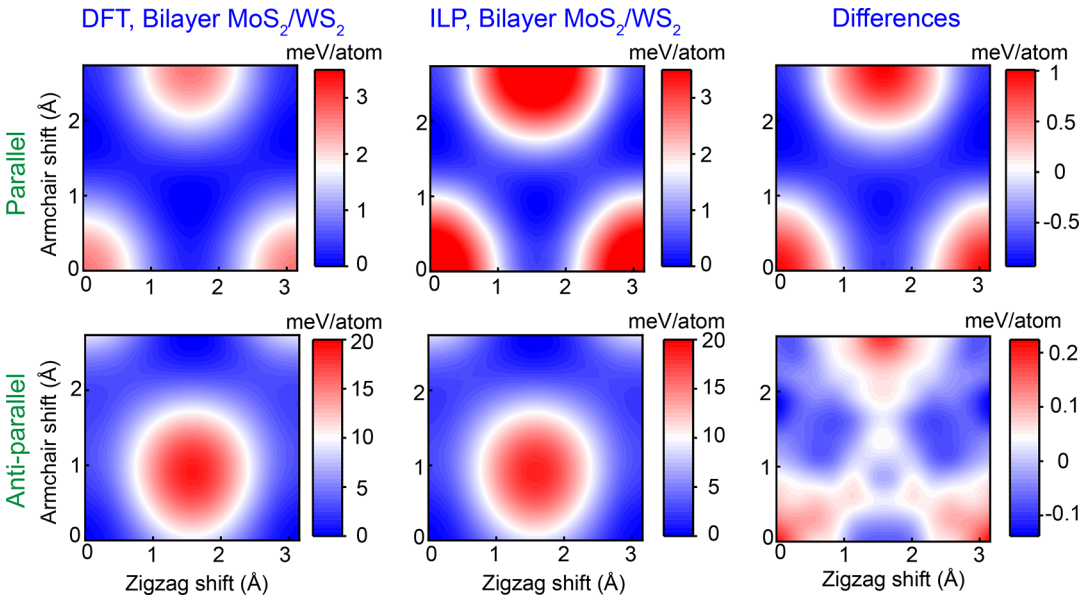

Figure 4. Sliding energy surfaces of bilayer MoS_2/WS_2, calculated at interlayer distances of 6.9 Å for the parallel (top panels) and 6.3 Å for the antiparallel (bottom panels) configurations. The left and middle columns present DFT (HSE + MBD-NL) and ILP PESs, respectively, and the right column presents their difference maps. The parameters presented in Table S1 in Supporting Information Section 3 are used for the ILP calculations. The reported energies are normalized by the total number of atoms in the unit-cell (6 atoms) and measured relative to the values obtained at the AB and AA′ stacking modes for the parallel and antiparallel configurations, respectively.

sufficient for a reliable parametrization of the interlayer interactions in the corresponding bulk systems.[28] Comparative test calculations, performed at the PBE + MBD-NL level of DFT, are presented in Supporting Information Section 5, suggesting that both approaches yield similar results.

2.2. Model Systems. Reference data and corresponding ILP parameters for Mo−Mo, Mo−S, and S−S were inherited from our previous work.[28] To obtain the rest of the parameters, we created reference data sets for all the three remaining homojunctions ($MoSe_2/MoSe_2$, WS_2/WS_2, and WSe_2/WSe_2) and two of the six possible heterojunctions ($MoS_2/MoSe_2$ and MoS_2/WS_2). The resulting ILP parametrization was then benchmarked against DFT calculations for the other heterojunctions, to test for accuracy and transferability of the parameters.

3. FORCE-FIELD PARAMETRIZATION

3.1. BE Curves. Figure 2 presents the calculated BE curves for the three bilayer homojunctions and the two chosen bilayer heterojunctions at the five high-symmetry stacking modes. In general, for all bilayer junctions considered, the BE curves can be divided into two groups: (i) AA and A′B stacking arrangements curves that present similar lower binding energies and larger equilibrium interlayer distances; (ii) AA′, AB, and AB′ stacking arrangements that show similar higher binding energies and smaller equilibrium interlayer distances. The BEs of the stacking modes appear in the following order: AA′ ≥ AB > AB′ > A′B ≥ AA, consistent with our previous results for MoS_2 and with independent PBE + D2 results.[61,62] We note that random phase approximation (RPA) calculations[35] predict a somewhat different order, where A′B is less stable than AA. The higher stability we obtain for the AA′ and AB stacking modes also agrees with the fact that they are the two natural forms (2*H* and 3*R* phases, respectively) of TMDs, where the former is more dominant, similar to the case of hexagonal boron nitride (*h*-BN). A quantitative analysis shows that DFT results for TMD bilayer equilibrium distances and binding energies, obtained at the level of HSE + MBD-NL, differ from RPA calculations[61] by ∼1.5% and 20.3% (calculated as the absolute difference between the RPA and DFT values relative to the RPA result), respectively (see Table 1). In comparison, vdW-DF-C09 was found to overestimate BEs by ∼40%.[26,56]

3.2. Sliding PESs. Figure 3 and 4 present the corresponding sliding PESs for the homogeneous $MoSe_2/MoSe_2$ and the heterogeneous MoS_2/WS_2 interfaces, calculated at their fixed equilibrium interlayer distances. The left columns present the DFT reference data for the parallel (panel a, starting from the AA stacking mode) and antiparallel (panel d, starting from the AA′ stacking mode) configurations. PESs for the other homo- and heterojunctions are provided in Supporting Information Section 2. In total, 25 BE curves and 10 sliding PESs serve as a reference data set in the ILP parametrization procedure.

3.3. Formula of the Interlayer Potential. The functional form of the ILP is the same as that used previously for MoS_2, graphene, and *h*-BN interfaces, namely:[22−25,27,28]

$$V(r_{ij}, \boldsymbol{n}_i, \boldsymbol{n}_j) = \mathrm{Tap}(\boldsymbol{r}_{ij})[V_{\mathrm{att}}(r_{ij}) + V_{\mathrm{rep}}(r_{ij}, \boldsymbol{n}_i, \boldsymbol{n}_j)] \quad (1)$$

Where,

$$V_{\mathrm{att}}(r_{ij}) = -\frac{1}{1 + e^{-d_{ij}[r_{ij}/(s_{R,ij}\cdot r_{ij}^{\mathrm{eff}})-1]}}\frac{C_{6,ij}}{r_{ij}^6} \quad (2)$$

is a long-range pairwise term that represents van der Waals attraction,

$$V_{\mathrm{rep}}(r_{ij}, \boldsymbol{n}_i, \boldsymbol{n}_j) = e^{\alpha_{ij}\left(1-\frac{r_{ij}}{\beta_{ij}}\right)}\{\varepsilon_{ij} + C_{ij}[e^{-(\rho_{ij}/\gamma_{ij})^2} + e^{-(\rho_{ji}/\gamma_{ij})^2}]\} \quad (3)$$

is a short-range registry-dependent term that represents Pauli repulsion, and

https://doi.org/10.1021/acs.jpca.3c04540
J. Phys. Chem. A 2023, 127, 9820−9830

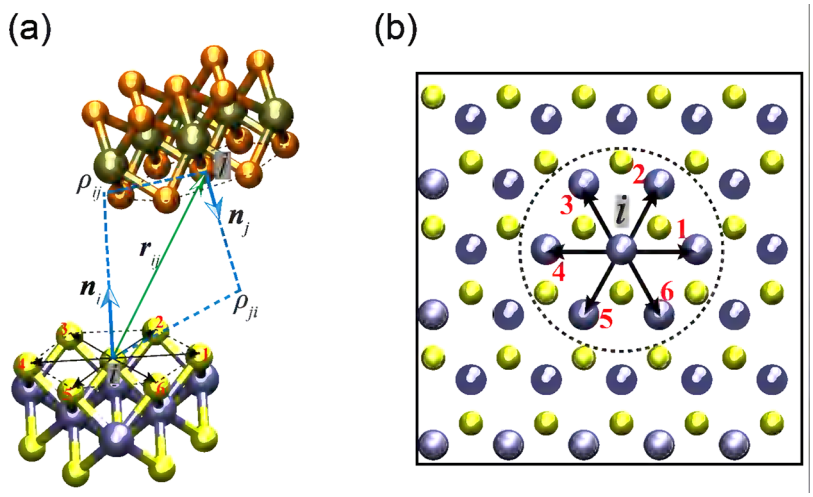

Figure 5. Illustration of the various distance vectors involved in the ILP expression. (a) Perspective view of a TMD bilayer showing the full interatomic distance vector $\boldsymbol{r}_{ij}$ between atom i residing in one layer and atom j residing in its adjacent layer, the local normal vectors, $\boldsymbol{n}_i$ and $\boldsymbol{n}_j$, and the lateral distances ρ_{ij} and ρ_{ji}. (b) Top view of the bottom TMD layer showing the six nearest neighboring atoms of atom i within the same TMD sublayer, used to define the corresponding local normal vector $\boldsymbol{n}_i$. The atomic false color scheme follows that used in Figure 1, where atoms residing in different layers are marked with different colors.

$$\mathrm{Tap}(r_{ij}) = 20\left(\frac{r_{ij}}{R_{\mathrm{cut}}}\right)^7 - 70\left(\frac{r_{ij}}{R_{\mathrm{cut}}}\right)^6 + 84\left(\frac{r_{ij}}{R_{\mathrm{cut}}}\right)^5 - 35\left(\frac{r_{ij}}{R_{\mathrm{cut}}}\right)^4 + 1 \tag{4}$$

is a taper function that smoothly reduces the potential and its derivatives (up to third order) to zero beyond an interatomic cutoff distance of R_{cut} = 16 Å. Here, $r_{ij} = |\boldsymbol{r}_{ij}|$ is the interatomic distance between atom i residing in one layer and atom j residing in its adjacent layer, $\boldsymbol{n}_i$ is the surface normal vector at the position of atom i calculated through its six nearest neighboring atoms residing in the same sublayer as atom i (out of the three sublayers of a given TMD layer, see Figure 5),

$$\boldsymbol{n}_i = \frac{\boldsymbol{N}_i}{|\boldsymbol{N}_i|}, \qquad \boldsymbol{N}_i = \frac{1}{6}\sum_{k=1}^{6}(\boldsymbol{r}_{k,i} \times \boldsymbol{r}_{k+1,i}) \tag{5}$$

where $\boldsymbol{r}_{k,i} = \boldsymbol{r}_k - \boldsymbol{r}_i$, k = 1,2,⋯, 6, and the summation is cyclic with $\boldsymbol{r}_{7,i} = \boldsymbol{r}_{1,i}$, $C_{6,ij}$ is the pairwise vdW attraction coefficient, r_{ij}^{eff} is the sum of the effective equilibrium vdW atomic radii, d_{ij} and $s_{R,ij}$ are unitless parameters determining the steepness and onset of the short-range Fermi−Dirac-type damping function, ε_{ij} and C_{ij} are constants that define the energy scales corresponding to the isotropic and anisotropic repulsions, respectively, β_{ij} and γ_{ij} set the associated interaction ranges, and α_{ij} is a parameter that sets the steepness of the isotropic repulsion function. Importantly, the anisotropic repulsive term depends not only on the pairwise distance, r_{ij}, but also on the lateral interatomic distance, $\rho_{ij}(\rho_{ji})$, calculated as the distance of atom $j(i)$ to the surface normal, $\boldsymbol{n}_i$ ($\boldsymbol{n}_j$), of atom $i(j)$ as shown in Figure 5:

$$\begin{cases} \rho_{ij}^2 = r_{ij}^2 - (\boldsymbol{r}_{ij}\cdot\boldsymbol{n}_i)^2 \\ \rho_{ji}^2 = r_{ji}^2 - (\boldsymbol{r}_{ji}\cdot\boldsymbol{n}_j)^2 \end{cases} \tag{6}$$

We note that interlayer Coulomb effects are found to be considerably weaker than van der Waals interactions in our systems (see Section 4 of the Supporting Information), thus Coulomb effects are ignored in the ILP formula of eq 1, thereby considerably reducing the computational burden.[30]

3.4. Fitting Protocol. In total, the ILP expression involves a set of nine pairwise parameters $\boldsymbol{\xi} = \{\alpha_{ij}, \beta_{ij}, \gamma_{ij}, \varepsilon_{ij}, C_{ij}, d_{ij}, s_{R,ij}, r_{ij}^{\mathrm{eff}}, C_{6,ij}\}$, where each parameter is symmetric with respect to index interchange due to the symmetry of the interaction. These parameters are fitted against the M = M_b + M_s (M_b = 25 BE curves and M_s = 10 sliding PESs) reference DFT data sets. For convenience, we denote the BE curves as $E_m^b(\boldsymbol{\xi})$, $m \in [1, 25]$, and the sliding PESs as $E_m^s(\boldsymbol{\xi})$, $m \in [1, 10]$. To balance the large energy variation in BE curves, especially in the subequilibrium regime, against the relatively low energy corrugation of the PESs, we define the following objective function:

$$\Phi(\boldsymbol{\xi}) = \sum_{m=1}^{M_b} w_m^b \| E_m^b(\boldsymbol{\xi}) - E_m^{b,\mathrm{DFT}} \|_2 + \sum_{m=1}^{M_s} w_m^s \| E_m^s(\boldsymbol{\xi}) - E_m^{s,\mathrm{DFT}} \|_2 \tag{7}$$

where the contributions of BE curves and sliding PESs are weighted with factors of w_m^b ($d < d_{\mathrm{eq}}^m$) = 1, w_m^b ($d \geq d_{\mathrm{eq}}^m$) = 40 and w_m^s = 100, respectively, where d is the interlayer distance, d_{eq}^m is its equilibrium value for the m^{th} BE curve, and $\|\cdots\|_2$ is the Euclidean norm (2-norm) that measures the difference between the ILP predictions and the DFT reference data. The ILP parameters are set by minimizing this objective function using an interior-point algorithm implemented in the MATLAB software suite.[63,64] Additional details pertaining to the fitting procedure can be found in refs. 25 and 27. The fitted parameters are provided in Supporting Information Section 3, along with the corresponding MoS_2 parameters obtained in our previous study.[28] The ILP obtained using this scheme provides very good agreement with the HSE + MBD-NL reference data for both BE curves (see Figure 2 and Table 1) and PESs (Figures 3, 4, and S3−S5). The maximal and average BE deviations among the five high symmetry stacking configurations depicted in Figure 1 are 1.91 and 0.63 meV/atom, respectively. The corresponding values for the PESs are 1.42

https://doi.org/10.1021/acs.jpca.3c04540
J. Phys. Chem. A 2023, 127, 9820−9830

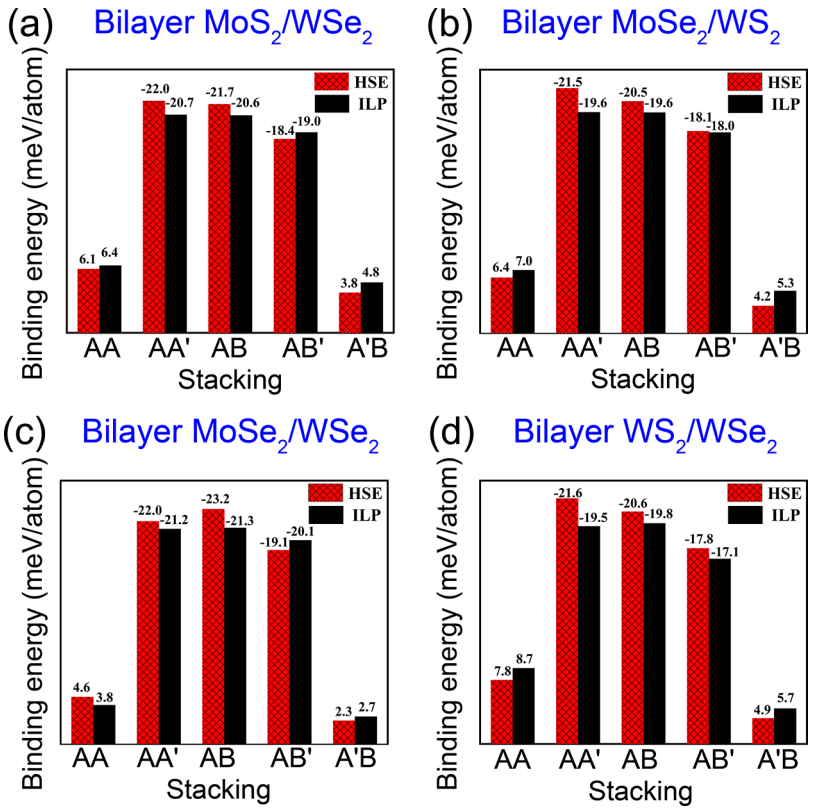

Figure 6. Transferability test of the developed ILP BEs, at high-symmetry stacking modes of the four bilayer heterojunctions deliberately excluded from the training set: (a) MoS_2/WSe_2; (b) $MoSe_2/WS_2$; (c) $MoSe_2/WSe_2$; (d) WS_2/WSe_2.

and 0.40 meV/atom, respectively (see Figures 3, 4 and S3–S5).

4. BENCHMARK TESTS

4.1. Transferability of the Parameters. As a test for the transferability of our ILP parametrizations, we compare the ILP BEs of the four bilayer heterojunctions not included in the reference data set to the corresponding HSE + MBD-NL values, obtained at the high-symmetry stacking modes presented in Figure 1. As shown in Figure 6, the parametrized ILP transfers well to heterojunctions outside its training set that involve the same TMD atom types, with a maximal BE deviation of 2.12 meV/atom and a corresponding average value of 0.96 meV/atom. Furthermore, the transferability of the ILP is demonstrated by comparing the BE curves and sliding PESs of homo- and heterojunctions that are outside the training set (see Section 5 of the Supporting Information).

4.2. Lattice Constants and Bulk Moduli. To further benchmark the parametrized ILP, we compare ILP-computed structural parameters, (a and c lattice vectors and volume, V) of bulk $MoSe_2$, WS_2, and WSe_2, and their dependence on hydrostatic pressure (P), to available experimental and first-principles results. To that end, we constructed supercells consisting of 12 rectangular layers stacked in the AA′ mode, with each layer containing 1250 M + 2500 X atoms. The initial values of the c lattice vector were set to 13.2, 12.8, and 13.2 Å for $MoSe_2$, WS_2, and WSe_2, respectively. The intra- and interlayer interactions were described by the Stillinger–Weber (SW)[65] potential and the parametrized ILP, respectively. All MD simulations were performed using the LAMMPS simulation package[66] with a time-step of 1 fs, and periodic boundary conditions applied in all three directions. A Nosé–Hoover thermostat with a time constant of 0.25 ps was employed to maintain the system temperature at T = 300 K. Hydrostatic pressure was adjusted by relaxing the simulation box dimensions using a Nosé–Hoover barostat with a time constant of 1.0 ps.[67,68] To obtain the c–P, a–P, and V–P curves (see Fig. S12 in Sec. 6 of the Supporting Information), the simulation systems were first equilibrated in the NPT ensemble at a temperature of T = 300 K and a fixed target pressure for 100 ps. Thereafter, structural parameters were computed by averaging over a subsequent simulation period of 100 ps. Bulk moduli were then obtained by fitting the calculated V–P curves (see Figure S12) with the Murnaghan equation of state (EOS):[69,70]

$$V(P)/V_0 = [1 + B_V'/B_V^0 \cdot P]^{-1/B_V'} \quad (8)$$

here, V_0 and $V(P)$ are the unit-cell volumes in the absence and presence of external hydrostatic pressure, and B_V^0 and B_V' are the bulk modulus and its pressure derivative at zero pressure, respectively. For completeness, bulk moduli were also calculated by fitting V–P curves with two other commonly used EOSs: (i) the Birch–Murnaghan equation[71,72] and (ii) the Vinet equation,[73,74] where B_V assumes a polynomial and exponential dependence on the pressure, instead of the linear dependence assumed in the Murnaghan EOS (see Supporting Information Section 6 for further details).

Figure 7 presents the ILP results and available literature data for the equilibrium structural parameters a_0 (top row) and c_0 (middle row) and bulk moduli (bottom row) for the three homojunctions considered. The a_0 parameter, which is mostly affected by the adopted intralayer SW potential, shows good agreement with experimental results and most of the dispersion-corrected DFT values, with deviations of 0.024,

https://doi.org/10.1021/acs.jpca.3c04540
J. Phys. Chem. A 2023, 127, 9820–9830

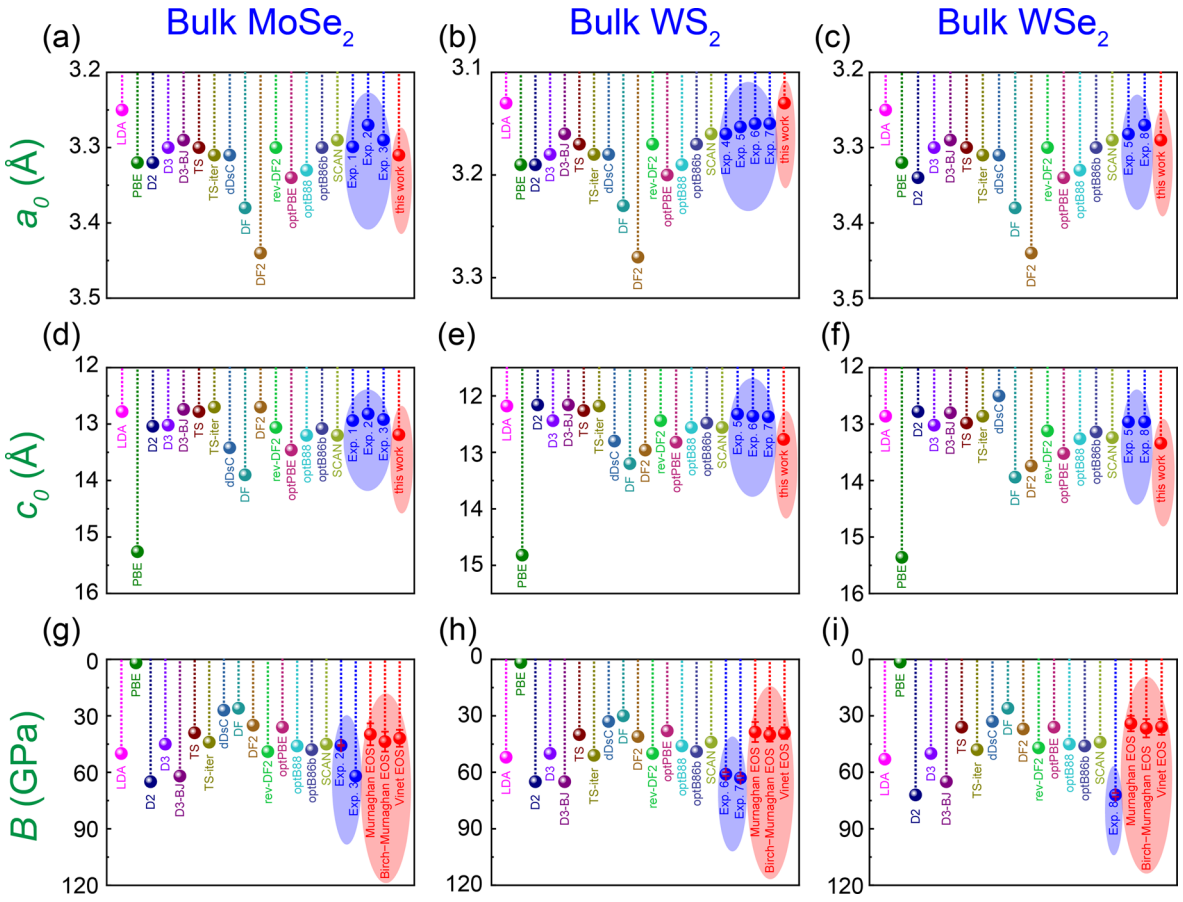

Figure 7. Comparison of ILP-computed a_0 (a–c), and c_0 (d–f) lattice parameters, and bulk moduli (g–i), with available experimental and DFT data for AA′-stacked bulk $MoSe_2$, WS_2, and WSe_2. Reported experimental values and our NPT simulation results are presented as blue and red circles, respectively. The error bars around the simulated data were obtained from the temporal standard deviation at equilibrium. In panels a–f, they are smaller than the symbol size. The DFT reference data are taken from ref. 75. The experimental reference data are extracted from ref. 76 (Exp. 1), ref. 77 (Exp. 2), ref. 78 (Exp. 3), ref. 79 (Exp. 4), ref. 80 (Exp. 5), ref. 81 (Exp. 6), ref. 82 (Exp. 7), and ref. 83 (Exp. 8), respectively.

0.023, and 0.014 Å from experiments (averaged over available measured data) for bulk $MoSe_2$, WS_2, and WSe_2, respectively. Similarly, the c_0 parameter, which is determined by the ILP, shows good agreement with both experimental results and most of the dispersion-corrected DFT values, with deviations of 0.297, 0.419, and 0.380 Å from experiments (averaged over available measured data) for bulk $MoSe_2$, WS_2, and WSe_2, respectively. As may be expected, despite the fact that LDA predictions agree well with the experimental values, which is known to be a result of fortuitous error cancellation, dispersion corrections to DFT are important for obtaining reliable interlayer lattice constants, as demonstrated by the significantly overestimated PBE values. The Murnaghan bulk moduli of $MoSe_2$, WS_2, and WSe_2 are 39.8 ± 5.8, 38.6 ± 5.3, and 34.1 ± 4.1 GPa, respectively. Similar values were obtained using the other EOSs (see Table S2 in Supporting Information Section 6). These values underestimate the experimental results by ∼19.5, 32.5, and 52.6%, respectively, and agree with most of the previous dispersion-corrected DFT results. We note that the same trends were also found for bulk MoS_2.

4.3. Phonon Spectra. For examining the accuracy of the ILP parametrizations, we use the parametrized ILP along with the intralayer SW potential to calculate the phonon spectra of the various homogeneous and heterogeneous junctions, which play a central role in their mechanical, thermal transport, and tribological properties. To that end, we follow the protocol described in refs. 27 and 28, where the dynamical matrix of the systems is first calculated in LAMMPS[66] with a numerical differentiation step size of 10^{-6} Å, then diagonalized to obtain the phonon spectrum. The supercell used in these calculations contains 25 × 25 × 6 unit cells (a total of 45,000 atoms). A grid of 201 points in reciprocal space was used to plot each branch of the phonon spectrum. Figure 8a,b presents the dispersion relations for bulk $MoSe_2$ and bulk alternating MoS_2/WS_2. The dispersion of the low energy out-of-plane branches (near the Γ point), which is related to the soft flexural modes of the layers and highlighted by green dotted rectangles (see Figure 8c,d), is mainly determined by the ILP, while the high energy modes depend mainly on the intralayer SW potential term. Notably, the isotropic Lennard-Jones (LJ) interlayer potential, parametrized by the universal force field,[84] considerably underestimates the out-of-plane phonon energies. Similar trends are found for the other bulk TMD systems considered (Supporting Information Section 7).

4.4. Atomic Reconstruction in Twisted TMD Bilayers. To further demonstrate the applicability of the parametrized ILP for the description of twisted TMD interfaces, which are not included in the reference DFT data set,[85] we evaluate its ability to capture the complex reconstructed moiré superstructures exhibited by twisted MoS_2 interfaces. To that end, we construct laterally periodic rectangular structures of twisted MoS_2 bilayers at both the parallel and antiparallel config-

https://doi.org/10.1021/acs.jpca.3c04540
J. Phys. Chem. A 2023, 127, 9820−9830

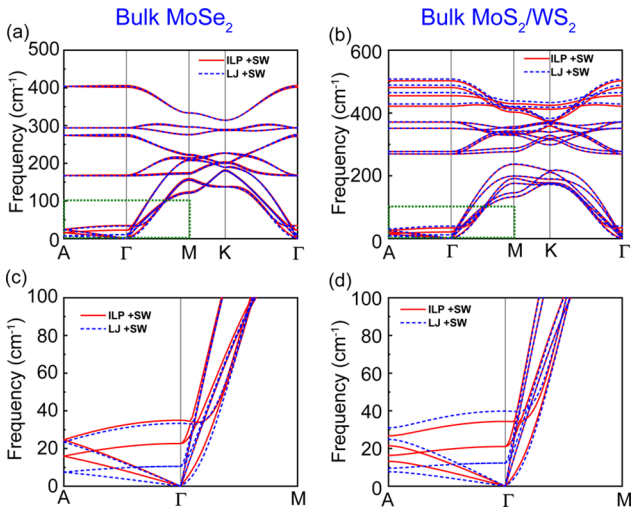

Figure 8. (a) Phonon spectra calculated using the ILP with the SW intralayer potential for (a) bulk $MoSe_2$ and (b) bulk alternating MoS_2/WS_2. Red solid lines are dispersion curves calculated using the parameters listed in Table S1. LJ results are presented for comparison by the blue dashed lines. Panels (c, d) show zoom-ins on the low-energy phonon modes near the Γ-point, marked by the dashed green rectangles in panels (a, b), respectively.

urations, and perform geometry optimization using the SW[65] potential and our ILP (both implemented in LAMMPS[66]) to describe the intra- and interlayer interactions, respectively. The optimization is performed in multiple steps to ensure structural relaxation and the release of residual stress. Initially, the atomic positions and the simulation box dimensions of the bilayer models are optimized using the "box/relax" keyword with the conjugated gradients (CG) minimization (a force convergence criterion of 10^{-6} eV $Å^{-1}$ is used throughout). This is followed by atomic position relaxation using the FIRE algorithm.[86] The above-mentioned geometry optimization process is repeated for 10 cycles to fully relax the box. To verify that the system does not get trapped in a local minimum, the whole system is heated to 300 K during 100,000 time steps using the Nosé–Hoover thermostat with a time-step of 0.25 fs, followed by thermal equilibration at 300 K and zero pressure for another 100,000 steps with a time-step of 1 fs, where the pressure is controlled by the Nosé–Hoover barostat. After these steps, the system is further optimized using the FIRE algorithm, followed by 10 more cycles of box relaxation using the CG algorithm. Finally, the system is optimized again using the FIRE algorithm. The optimization procedure described above ensures full relaxation of the residual stress in the considered structures.

As shown in Figure 9, the parametrized ILP used in conjunction with conventional intralayer force fields reproduces well the experimentally observed atomic reconstruction patterns in twisted MoS_2.[85] Specifically, the triangular and hexagonal moiré superlattice patterns exhibited by parallel and antiparallel twisted MoS_2 reconstructed bilayers, respectively, are nicely captured. These results strongly support the validity of our parametrized ILP to describe twisted TMD interfaces.

5. CONCLUSIONS

In conclusion, the benchmark tests presented above demonstrate the validity range of the developed ILP for group-VI layered TMD systems of the formula MX_2, where M = Mo, W,

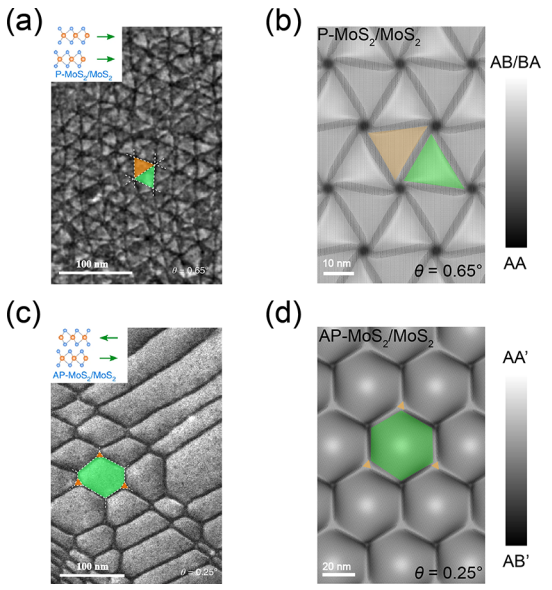

Figure 9. Comparison of experimentally observed and computed MoS_2 bilayer reconstructed superstructures. (a, c) Filtered annular dark-field scanning transmission electron microscopy images of suspended twisted MoS_2 bilayers stacked in the parallel (a) and antiparallel (c) configurations with twist angles of $\theta = 0.65°$ and $\theta = 0.25°$, respectively. (b, d) Local registry index[87] corrugation (gray scale) of twisted MoS_2 bilayers in the parallel configuration with $\theta = 0.65°$ (b) and the antiparallel configuration with $\theta = 0.25°$ (d), relaxed using the parametrized ILP. Colored panes highlight different types of domains. The yellow and green markings stand for AB and BA stacks in panel (b) and the AA′ and A′B stacks in panel (d), respectively. Panels (a) and (c) are adapted, with permission, from ref. 85. Copyright 2020 Springer Nature.

and X = S, Se. The force-field parametrization against reference data sets, obtained using screened hybrid DFT augmented by nonlocal many-body dispersion corrections, yields good agreement with experimental lattice parameters and is found to be transferable to TMD interfaces outside the training set that contain the same type of atoms. The calculated bulk moduli agree with most previous dispersion-augmented DFT predictions, which underestimate available experimental values. The successful construction of a registry-dependent interlayer potential based on state-of-the-art many-body dispersion-corrected DFT reference data for homogeneous and heterogeneous TMD interfaces opens the way for efficient yet accurate large-scale simulations of their dynamical, tribological, and heat transport properties.

■ ASSOCIATED CONTENT

Supporting Information

The Supporting Information is available free of charge at https://pubs.acs.org/doi/10.1021/acs.jpca.3c04540.

Convergence tests of the reference DFT calculations; additional sliding PESs; interlayer potential parameters; importance of Coulomb interactions; transferability of the developed ILPs; bulk moduli fitting; and phonon spectra for additional junctions (PDF)

■ AUTHOR INFORMATION

Corresponding Authors

Wengen Ouyang − *Department of Engineering Mechanics, School of Civil Engineering, Wuhan University, Wuhan,*

https://doi.org/10.1021/acs.jpca.3c04540
J. Phys. Chem. A 2023, 127, 9820−9830

Hubei 430072, China; State Key Laboratory of Water Resources and Hydropower Engineering Science, Wuhan University, Wuhan 430072, China; orcid.org/0000-0001-8700-1978; Email: w.g.ouyang@whu.edu.cn

Michael Urbakh − *School of Chemistry and The Sackler Center for Computational Molecular and Materials Science, Tel Aviv University, Tel Aviv 6997801, Israel;* Email: urbakh@tauex.tau.ac.il

Authors

Wenwu Jiang − *Department of Engineering Mechanics, School of Civil Engineering, Wuhan University, Wuhan, Hubei 430072, China*

Reut Sofer − *School of Chemistry and The Sackler Center for Computational Molecular and Materials Science, Tel Aviv University, Tel Aviv 6997801, Israel*

Xiang Gao − *School of Chemistry and The Sackler Center for Computational Molecular and Materials Science, Tel Aviv University, Tel Aviv 6997801, Israel;* orcid.org/0000-0002-8229-2865

Alexandre Tkatchenko − *Department of Physics and Materials Science, University of Luxembourg, L-1511 Luxembourg City, Luxembourg;* orcid.org/0000-0002-1012-4854

Leeor Kronik − *Department of Molecular Chemistry and Materials Science, Weizmann Institute of Science, Rehovoth 76100, Israel;* orcid.org/0000-0001-6791-8658

Oded Hod − *School of Chemistry and The Sackler Center for Computational Molecular and Materials Science, Tel Aviv University, Tel Aviv 6997801, Israel;* orcid.org/0000-0003-3790-8613

Complete contact information is available at: https://pubs.acs.org/10.1021/acs.jpca.3c04540

Author Contributions

¶W.J., R.S., and X.G. contributed equally to this work.

Notes

The authors declare no competing financial interest.

■ ACKNOWLEDGMENTS

W.O. acknowledges the financial support from the National Natural Science Foundation of China (nos. 12102307, 11890673, and 11890674), the National Natural Science Foundation of Hubei Province (2021CFB138), the Key Research and Development Program of Hubei Province (no. 2021BAA192), the Fundamental Research Funds for the Central Universities (no. 2042022kf1177), and the start-up fund of Wuhan University. X.G. acknowledges the postdoctoral fellowships of the Sackler Center for Computational Molecular and Materials Science and Ratner Center for Single Molecule Science at Tel Aviv University. M.U. acknowledges the financial support of the Israel Science Foundation, grant no. 1141/18 and the ISF-NSFC joint grant 3191/19. O.H. is grateful for the generous financial support of the Israel Science Foundation under grant no. 1586/17, the Heineman Chair in Physical Chemistry, Tel Aviv University Center for Nanoscience and Nanotechnology, and the Naomi Foundation for generous financial support via the 2017 Kadar Award. L.K. thanks the Aryeh and Mintzi Katzman Professorial Chair and the Helen and Martin Kimmel Award for Innovative Investigation. Computations were conducted at the National Supercomputer TianHe-1(A) Center in Tianjin and the Supercomputing Center of Wuhan University.

■ REFERENCES

(1) Manzeli, S.; Ovchinnikov, D.; Pasquier, D.; Yazyev, O. V.; Kis, A. 2D transition metal dichalcogenides. *Nat. Rev. Mater.* **2017**, *2* (8), 17033.

(2) Zhang, Z.; Wang, Y.; Watanabe, K.; Taniguchi, T.; Ueno, K.; Tutuc, E.; LeRoy, B. J. Flat bands in twisted bilayer transition metal dichalcogenides. *Nat. Phys.* **2020**, *16* (11), 1093−1096.

(3) Weston, A.; Zou, Y.; Enaldiev, V.; Summerfield, A.; Clark, N.; Zólyomi, V.; Graham, A.; Yelgel, C.; Magorrian, S.; Zhou, M.; et al. Atomic reconstruction in twisted bilayers of transition metal dichalcogenides. *Nat. Nanotechnol.* **2020**, *15*, 592−597.

(4) Rosenberger, M. R.; Chuang, H.-J.; Phillips, M.; Oleshko, V. P.; McCreary, K. M.; Sivaram, S. V.; Hellberg, C. S.; Jonker, B. T. Twist Angle-Dependent Atomic Reconstruction and Moiré Patterns in Transition Metal Dichalcogenide Heterostructures. *ACS Nano* **2020**, *14* (4), 4550−4558.

(5) Chu, Z.; Regan, E. C.; Ma, X.; Wang, D.; Xu, Z.; Utama, M. I. B.; Yumigeta, K.; Blei, M.; Watanabe, K.; Taniguchi, T.; et al. Nanoscale Conductivity Imaging of Correlated Electronic States in WSe_2/WS_2 Moiré Superlattices. *Phys. Rev. Lett.* **2020**, *125*, 186803.

(6) Zhang, C.; Chuu, C.-P.; Ren, X.; Li, M.-Y.; Li, L.-J.; Jin, C.; Chou, M.-Y.; Shih, C.-K. Interlayer couplings, Moiré patterns, and 2D electronic superlattices in MoS_2/WSe_2 hetero-bilayers. *Sci. Adv.* **2017**, *3* (1), No. e1601459.

(7) Jin, C.; Regan, E. C.; Yan, A.; Iqbal Bakti Utama, M.; Wang, D.; Zhao, S.; Qin, Y.; Yang, S.; Zheng, Z.; Shi, S.; et al. Observation of Moiré excitons in WSe_2/WS_2 heterostructure superlattices. *Nature* **2019**, *567* (7746), 76−80.

(8) Karni, O.; Barré, E.; Lau, S. C.; Gillen, R.; Ma, E. Y.; Kim, B.; Watanabe, K.; Taniguchi, T.; Maultzsch, J.; Barmak, K.; et al. Infrared Interlayer Exciton Emission in MoS_2/WSe_2 Heterostructures. *Phys. Rev. Lett.* **2019**, *123* (24), 247402.

(9) Liu, H.; Wang, C.; Zuo, Z.; Liu, D.; Luo, J. Direct Visualization of Exciton Transport in Defective Few-Layer WS_2 by Ultrafast Microscopy. *Adv. Mater.* **2020**, *32* (2), 1906540.

(10) Kim, S. E.; Mujid, F.; Rai, A.; Eriksson, F.; Suh, J.; Poddar, P.; Ray, A.; Park, C.; Fransson, E.; Zhong, Y.; et al. Extremely anisotropic van der Waals thermal conductors. *Nature* **2021**, *597*, 660−665.

(11) Yan, Y.; Ding, S.; Wu, X.; Zhu, J.; Feng, D.; Yang, X.; Li, F. Tuning the physical properties of ultrathin transition-metal dichalcogenides via strain engineering. *RSC Adv.* **2020**, *10* (65), 39455−39467.

(12) Lin, M.-L.; Tan, Q.-H.; Wu, J.-B.; Chen, X.-S.; Wang, J.-H.; Pan, Y.-H.; Zhang, X.; Cong, X.; Zhang, J.; Ji, W.; et al. Moiré Phonons in Twisted Bilayer MoS_2. *ACS Nano* **2018**, *12*, 8770−8780.

(13) Kandemir, A.; Yapicioglu, H.; Kinaci, A.; Çağın, T.; Sevik, C. Thermal transport properties of MoS_2 and $MoSe_2$ monolayers. *Nanotechnology* **2016**, *27* (5), 055703.

(14) Wei, Z.; Liu, B.; Liu, C.; Bi, K.; Yang, J.; Chen, Y. Cross-plane phonon transport properties of molybdenum disulphide. *J. Phys. D: Appl. Phys.* **2015**, *48* (46), 465303.

(15) Li, H.; Wang, J.; Gao, S.; Chen, Q.; Peng, L.; Liu, K.; Wei, X. Superlubricity between MoS2 Monolayers. *Adv. Mater.* **2017**, *29* (27), 1701474.

(16) Vazirisereshk, M. R.; Hasz, K.; Zhao, M.-Q.; Johnson, A. T. C.; Carpick, R. W.; Martini, A. Nanoscale Friction Behavior of Transition-Metal Dichalcogenides: Role of the Chalcogenide. *ACS Nano* **2020**, *14* (11), 16013−16021.

(17) Vazirisereshk, M. R.; Hasz, K.; Carpick, R. W.; Martini, A. Friction Anisotropy of MoS_2: Effect of Tip-Sample Contact Quality. *J. Phys. Chem. Lett.* **2020**, *11* (16), 6900−6906.

(18) Berman, D.; Erdemir, A.; Sumant, A. V. Approaches for Achieving Superlubricity in Two-Dimensional Materials. *ACS Nano* **2018**, *12* (3), 2122−2137.

(19) Hod, O.; Meyer, E.; Zheng, Q.; Urbakh, M. Structural superlubricity and ultralow friction across the length scales. *Nature* **2018**, *563* (7732), 485−492.
(20) Kolmogorov, A. N.; Crespi, V. H. Registry-dependent interlayer potential for graphitic systems. *Phys. Rev. B: Condens. Matter Mater. Phys.* **2005**, *71* (23), 235415.
(21) Lebedeva, I. V.; Knizhnik, A. A.; Popov, A. M.; Lozovik, Y. E.; Potapkin, B. V. Interlayer interaction and relative vibrations of bilayer graphene. *Phys. Chem. Chem. Phys.* **2011**, *13* (13), 5687−5695.
(22) Leven, I.; Azuri, I.; Kronik, L.; Hod, O. Inter-layer potential for hexagonal boron nitride. *J. Chem. Phys.* **2014**, *140* (10), 104106.
(23) Leven, I.; Maaravi, T.; Azuri, I.; Kronik, L.; Hod, O. Interlayer Potential for Graphene/*h*-BN Heterostructures. *J. Chem. Theory Comput.* **2016**, *12* (6), 2896−2905.
(24) Maaravi, T.; Leven, I.; Azuri, I.; Kronik, L.; Hod, O. Interlayer Potential for Homogeneous Graphene and Hexagonal Boron Nitride Systems: Reparametrization for Many-Body Dispersion Effects. *J. Phys. Chem. C* **2017**, *121* (41), 22826−22835.
(25) Ouyang, W.; Mandelli, D.; Urbakh, M.; Hod, O. Nanoserpents: Graphene Nanoribbon Motion on Two-Dimensional Hexagonal Materials. *Nano Lett.* **2018**, *18* (9), 6009−6016.
(26) Naik, M. H.; Maity, I.; Maiti, P. K.; Jain, M. Kolmogorov-Crespi Potential for Multilayer Transition-Metal Dichalcogenides: Capturing Structural Transformations in Moiré Superlattices. *J. Phys. Chem. C* **2019**, *123*, 9770−9778.
(27) Ouyang, W.; Azuri, I.; Mandelli, D.; Tkatchenko, A.; Kronik, L.; Urbakh, M.; Hod, O. Mechanical and Tribological Properties of Layered Materials under High Pressure: Assessing the Importance of Many-Body Dispersion Effects. *J. Chem. Theory Comput.* **2020**, *16*, 666−676.
(28) Ouyang, W.; Sofer, R.; Gao, X.; Hermann, J.; Tkatchenko, A.; Kronik, L.; Urbakh, M.; Hod, O. Anisotropic Interlayer Force Field for Transition Metal Dichalcogenides: The Case of Molybdenum Disulfide. *J. Chem. Theory Comput.* **2021**, *17* (11), 7237−7245.
(29) Cooper, V. R. Van der Waals density functional: An appropriate exchange functional. *Phys. Rev. B: Condens. Matter Mater. Phys.* **2010**, *81* (16), 161104.
(30) Grimme, S. Semiempirical GGA-type density functional constructed with a long-range dispersion correction. *J. Comput. Chem.* **2006**, *27* (15), 1787−1799.
(31) Wu, X.; Vargas, M. C.; Nayak, S.; Lotrich, V.; Scoles, G. Towards extending the applicability of density functional theory to weakly bound systems. *J. Chem. Phys.* **2001**, *115* (19), 8748−8757.
(32) Tkatchenko, A.; Scheffler, M. Accurate Molecular Van Der Waals Interactions from Ground-State Electron Density and Free-Atom Reference Data. *Phys. Rev. Lett.* **2009**, *102* (7), 073005.
(33) Tkatchenko, A.; DiStasio, R. A.; Car, R.; Scheffler, M. Accurate and Efficient Method for Many-Body van der Waals Interactions. *Phys. Rev. Lett.* **2012**, *108* (23), 236402.
(34) Ambrosetti, A.; Reilly, A. M.; DiStasio, R. A., Jr; Tkatchenko, A. Long-range correlation energy calculated from coupled atomic response functions. *J. Chem. Phys.* **2014**, *140* (18), 18A508.
(35) Hermann, J.; Tkatchenko, A. Density Functional Model for van der Waals Interactions: Unifying Many-Body Atomic Approaches with Nonlocal Functionals. *Phys. Rev. Lett.* **2020**, *124* (14), 146401.
(36) Leven, I.; Guerra, R.; Vanossi, A.; Tosatti, E.; Hod, O. Multiwalled nanotube faceting unravelled. *Nat. Nanotechnol.* **2016**, *11*, 1082−1086.
(37) Liu, M.; Cowley, J. M. Structures of the helical carbon nanotubes. *Carbon* **1994**, *32* (3), 393−403.
(38) Gogotsi, Y.; Libera, J. A.; Kalashnikov, N.; Yoshimura, M. Graphite Polyhedral Crystals. *Science* **2000**, *290* (5490), 317−320.
(39) Garel, J.; Leven, I.; Zhi, C.; Nagapriya, K. S.; Popovitz-Biro, R.; Golberg, D.; Bando, Y.; Hod, O.; Joselevich, E. Ultrahigh Torsional Stiffness and Strength of Boron Nitride Nanotubes. *Nano Lett.* **2012**, *12* (12), 6347−6352.
(40) Lynch, R. W.; Drickamer, H. G. Effect of high pressure on the lattice parameters of diamond, graphite, and hexagonal boron nitride. *J. Chem. Phys.* **1966**, *44* (1), 181−184.
(41) Hanfland, M.; Beister, H.; Syassen, K. Graphite under pressure: Equation of state and first-order Raman modes. *Phys. Rev. B: Condens. Matter Mater. Phys.* **1989**, *39* (17), 12598−12603.
(42) Solozhenko, V. L.; Will, G.; Elf, F. Isothermal compression of hexagonal graphite-like boron nitride up to 12 GPa. *Solid State Commun.* **1995**, *96* (1), 1−3.
(43) Mandelli, D.; Leven, I.; Hod, O.; Urbakh, M. Sliding friction of graphene/hexagonal-boron nitride heterojunctions: a route to robust superlubricity. *Sci. Rep.* **2017**, *7* (1), 10851.
(44) Song, Y.; Mandelli, D.; Hod, O.; Urbakh, M.; Ma, M.; Zheng, Q. Robust microscale superlubricity in graphite/hexagonal boron nitride layered heterojunctions. *Nat. Mater.* **2018**, *17* (10), 894−899.
(45) Mandelli, D.; Ouyang, W.; Hod, O.; Urbakh, M. Negative Friction Coefficients in Superlubric Graphite-Hexagonal Boron Nitride Heterojunctions. *Phys. Rev. Lett.* **2019**, *122* (7), 076102.
(46) Ouyang, W.; Hod, O.; Urbakh, M. Registry-Dependent Peeling of Layered Material Interfaces: The Case of Graphene Nanoribbons on Hexagonal Boron Nitride. *ACS Appl. Mater. Interfaces* **2021**, *13* (36), 43533−43539.
(47) Gao, X.; Ouyang, W.; Hod, O.; Urbakh, M. Mechanisms of frictional energy dissipation at graphene grain boundaries. *Phys. Rev. B* **2021**, *103* (4), 045418.
(48) Gao, X.; Ouyang, W.; Urbakh, M.; Hod, O. Superlubric polycrystalline graphene interfaces. *Nat. Commun.* **2021**, *12* (1), 5694.
(49) Zhang, S.; Yao, Q.; Chen, L.; Jiang, C.; Ma, T.; Wang, H.; Feng, X.-Q.; Li, Q. Dual-Scale Stick-Slip Friction on Graphene/*h*-BN Moiré Superlattice Structure. *Phys. Rev. Lett.* **2022**, *128* (22), 226101.
(50) Huang, K.; Qin, H.; Zhang, S.; Li, Q.; Ouyang, W.; Liu, Y. The Origin of Moiré-Level Stick-Slip Behavior on Graphene/*h*-BN Heterostructures. *Adv. Funct. Mater.* **2022**, *32* (35), 2204209.
(51) Gao, X.; Urbakh, M.; Hod, O. Stick-Slip Dynamics of Moiré Superstructures in Polycrystalline 2D Material Interfaces. *Phys. Rev. Lett.* **2022**, *129* (27), 276101.
(52) Wirtz, L.; Rubio, A. The phonon dispersion of graphite revisited. *Solid State Commun.* **2004**, *131* (3−4), 141−152.
(53) Serrano, J.; Bosak, A.; Arenal, R.; Krisch, M.; Watanabe, K.; Taniguchi, T.; Kanda, H.; Rubio, A.; Wirtz, L. Vibrational Properties of Hexagonal Boron Nitride: Inelastic X-Ray Scattering and Ab Initio Calculations. *Phys. Rev. Lett.* **2007**, *98* (9), 095503.
(54) Ouyang, W.; Qin, H.; Urbakh, M.; Hod, O. Controllable Thermal Conductivity in Twisted Homogeneous Interfaces of Graphene and Hexagonal Boron Nitride. *Nano Lett.* **2020**, *20* (10), 7513−7518.
(55) Leven, I.; Krepel, D.; Shemesh, O.; Hod, O. Robust Superlubricity in Graphene/*h*-BN Heterojunctions. *J. Phys. Chem. Lett.* **2013**, *4* (1), 115−120.
(56) Hamada, I.; Otani, M. Comparative van der Waals density-functional study of graphene on metal surfaces. *Phys. Rev. B: Condens. Matter Mater. Phys.* **2010**, *82* (15), 153412.
(57) Yu, J.; Han, E.; Hossain, M. A.; Watanabe, K.; Taniguchi, T.; Ertekin, E.; van der Zande, A. M.; Huang, P. Y. Designing the Bending Stiffness of 2D Material Heterostructures. *Adv. Mater.* **2021**, *33* (9), No. e2007269.
(58) Blum, V.; Gehrke, R.; Hanke, F.; Havu, P.; Havu, V.; Ren, X.; Reuter, K.; Scheffler, M. Ab initio molecular simulations with numeric atom-centered orbitals. *Comput. Phys. Commun.* **2009**, *180* (11), 2175−2196.
(59) Krukau, A. V.; Vydrov, O. A.; Izmaylov, A. F.; Scuseria, G. E. Influence of the exchange screening parameter on the performance of screened hybrid functionals. *J. Chem. Phys.* **2006**, *125* (22), 224106.
(60) Havu, V.; Blum, V.; Havu, P.; Scheffler, M. Efficient integration for all-electron electronic structure calculation using numeric basis functions. *J. Comput. Phys.* **2009**, *228* (22), 8367−8379.
(61) He, J.; Hummer, K.; Franchini, C. Stacking effects on the electronic and optical properties of bilayer transition metal dichalcogenides MoS_2, $MoSe_2$, WS_2, and WSe_2. *Phys. Rev. B: Condens. Matter Mater. Phys.* **2014**, *89* (7), 075409.

https://doi.org/10.1021/acs.jpca.3c04540
J. Phys. Chem. A 2023, 127, 9820−9830

(62) Tao, P.; Guo, H.-H.; Yang, T.; Zhang, Z.-D. Stacking stability of MoS_2 bilayer: An ab initio study. *Chin. Phys. B* **2014**, *23* (10), 106801.
(63) Byrd, R. H.; Gilbert, J. C.; Nocedal, J. A trust region method based on interior point techniques for nonlinear programming. *Math. Program.* **2000**, *89* (1), 149−185.
(64) Waltz, R. A.; Morales, J. L.; Nocedal, J.; Orban, D. An interior algorithm for nonlinear optimization that combines line search and trust region steps. *Math. Program.* **2006**, *107* (3), 391−408.
(65) Jiang, J.-W. Misfit Strain-Induced Buckling for Transition-Metal Dichalcogenide Lateral Heterostructures: A Molecular Dynamics Study. *Acta Mech. Solida Sin.* **2019**, *32* (1), 17−28.
(66) Plimpton, S. Fast Parallel Algorithms for Short-Range Molecular Dynamics. *J. Comput. Phys.* **1995**, *117* (1), 1−19.
(67) Shinoda, W.; Shiga, M.; Mikami, M. Rapid estimation of elastic constants by molecular dynamics simulation under constant stress. *Phys. Rev. B: Condens. Matter Mater. Phys.* **2004**, *69* (13), 134103.
(68) O'Connor, T. C.; Andzelm, J.; Robbins, M. O. AIREBO-M: A reactive model for hydrocarbons at extreme pressures. *J. Chem. Phys.* **2015**, *142* (2), 024903.
(69) Murnaghan, F. D. The Compressibility of Media under Extreme Pressures. *Proc. Natl. Acad. Sci. U.S.A.* **1944**, *30* (9), 244−247.
(70) Hanfland, M.; Beister, H.; Syassen, K. Graphite under pressure: Equation of state and first-order Raman modes. *Phys. Rev. B: Condens. Matter Mater. Phys.* **1989**, *39* (17), 12598−12603.
(71) Birch, F. Finite Elastic Strain of Cubic Crystals. *Phys. Rev.* **1947**, *71* (11), 809−824.
(72) Birch, F. Elasticity and constitution of the Earth's interior. *J. Geophys. Res.* **1952**, *57* (2), 227−286.
(73) Vinet, P.; Ferrante, J.; Smith, J. R.; Rose, J. H. A universal equation of state for solids. *J. Phys. C: Solid State Phys.* **1986**, *19* (20), L467−L473.
(74) Vinet, P.; Smith, J. R.; Ferrante, J.; Rose, J. H. Temperature effects on the universal equation of state of solids. *Phys. Rev. B: Condens. Matter Mater. Phys.* **1987**, *35* (4), 1945−1953.
(75) Pisarra, M.; Díaz, C.; Martín, F. Theoretical study of structural and electronic properties of 2*H*-phase transition metal dichalcogenides. *Phys. Rev. B* **2021**, *103* (19), 195416.
(76) Böker, T.; Severin, R.; Muller, A.; Janowitz, C.; Manzke, R.; Voß, D.; Kruger, P.; Mazur, A.; Pollmann, J. Band structure of MoS_2, $MoSe_2$, and α-MoS_2: Angle-resolved photoelectron spectroscopy and ab initio calculations. *Phys. Rev. B: Condens. Matter Mater. Phys.* **2001**, *64* (23), 235305.
(77) Aksoy, R.; Selvi, E.; Ma, Y. X-ray diffraction study of molybdenum diselenide to 35.9 GPa. *J. Phys. Chem. Solids* **2008**, *69* (9), 2138−2140.
(78) Zhao, Z.; Zhang, H.; Yuan, H.; Wang, S.; Lin, Y.; Zeng, Q.; Xu, G.; Liu, Z.; Solanki, G. K.; Patel, K. D.; et al. Pressure induced metallization with absence of structural transition in layered molybdenum diselenide. *Nat. Commun.* **2015**, *6* (1), 7312.
(79) Bromley, R. A.; Murray, R. B.; Yoffe, A. D. The band structures of some transition metal dichalcogenides. III. Group VIA: trigonal prism materials. *J. Phys. C: Solid State Phys.* **1972**, *5* (7), 759−778.
(80) Schutte, W. J.; De Boer, J. L.; Jellinek, F. Crystal structures of tungsten disulfide and diselenide. *J. Solid State Chem.* **1987**, *70* (2), 207−209.
(81) Selvi, E.; Ma, Y.; Aksoy, R.; Ertas, A.; White, A. High pressure X-ray diffraction study of tungsten disulfide. *J. Phys. Chem. Solids* **2006**, *67* (9−10), 2183−2186.
(82) Bandaru, N.; Kumar, R. S.; Baker, J.; Tschauner, O.; Hartmann, T.; Zhao, Y.; Venkat, R. Structural stability of WS_2 under high pressure. *Int. J. Mod. Phys. B* **2014**, *28* (25), 1450168.
(83) Selvi, E.; Aksoy, R.; Knudson, R.; Ma, Y. High-pressure X-ray diffraction study of tungsten diselenide. *J. Phys. Chem. Solids* **2008**, *69* (9), 2311−2314.
(84) Rappe, A. K.; Casewit, C. J.; Colwell, K. S.; Goddard, W. A., III; Skiff, W. M. UFF, a full periodic table force field for molecular mechanics and molecular dynamics simulations. *J. Am. Chem. Soc.* **1992**, *114* (25), 10024−10035.
(85) Weston, A.; Zou, Y.; Enaldiev, V.; Summerfield, A.; Clark, N.; Zolyomi, V.; Graham, A.; Yelgel, C.; Magorrian, S.; Zhou, M.; et al. Atomic reconstruction in twisted bilayers of transition metal dichalcogenides. *Nat. Nanotechnol.* **2020**, *15* (7), 592−597.
(86) Bitzek, E.; Koskinen, P.; Gahler, F.; Moseler, M.; Gumbsch, P. Structural relaxation made simple. *Phys. Rev. Lett.* **2006**, *97* (17), 170201.
(87) Cao, W.; Hod, O.; Urbakh, M. Interlayer Registry Index of Layered Transition Metal Dichalcogenides. *J. Phys. Chem. Lett.* **2022**, *13* (15), 3353−3359.

https://doi.org/10.1021/acs.jpca.3c04540
J. Phys. Chem. A 2023, 127, 9820−9830